

Infra-red emission line tomography of the intergalactic medium during the Epoch of Reionization

Koki Kakiichi, Avery Meiksin, Eric Tittley

*SUPA**, *Institute for Astronomy, University of Edinburgh, Blackford Hill, Edinburgh EH9 3HJ, UK*

10 July 2018

ABSTRACT

The first major star-forming galaxies and Active Galactic Nuclei will produce Balmer and higher order extended haloes during the Epoch of Reionization through the scattering of Lyman resonance line photons off the surrounding neutral intergalactic gas. The optical depth dependence of the scattering rates will produce a signal sensitive to both the density and velocity fluctuations of the gas, offering the possibility of probing the ionization region and flow field surrounding young star-forming galaxies. The requirements for detecting the haloes in the infra-red using a space-based telescope are discussed, along with an assessment of the possibility of detecting the haloes using the Tunable Filter Imager on the *James Webb Space Telescope*.

Key words: atomic processes – cosmology: theory – line: formation – radiative transfer – infrared: general – scattering

1 INTRODUCTION

The breaking of the redshift $z = 7$ barrier in the campaign to discover high redshift galaxies is closing in on the Epoch of Reionization (EoR), when sufficient stars, with a possible contribution from Active Galactic Nuclei (AGN), formed to reionize the hydrogen produced in the Big Bang following the Recombination Era. In addition to the handful of sources with spectroscopically confirmed redshifts $z > 7$ (Vanzella et al. 2011; Ono et al. 2012; Schenker et al. 2012), several plausible candidates have been identified with higher photometric redshifts extending up to $z \lesssim 9$ (McLure et al. 2011), and possibly as high as $z \simeq 10$ (Bouwens et al. 2011). Measurements of the Cosmic Microwave Background (CMB) by the *Wilkinson Microwave Anisotropy Probe* (WMAP) confine the EoR, if a sudden event, to $z_r = 10.4 \pm 1.2$ (1σ) (Larson et al. 2011). Thus the highest redshift galaxies discovered may have already entered the EoR.

In addition to ionizing the IGM, high redshift galaxies will illuminate still neutral intergalactic hydrogen before the EoR has ended. The Ly α radiation escaping high redshift sources will scatter in the vicinity of the sources, producing Ly α haloes with a characteristic core radius of 70 kpc at $z = 10$ (Loeb & Rybicki 1999). These haloes would be observable in the near infra-red, with characteristic diameters of 30 arcsecs. The sources will be overwhelmed by zodiacal light, but a dedicated space-based facility with narrow band imaging could plausibly detect a halo surrounding a very bright source.

Higher energy photons emitted by the continuum of the sources will scatter as well as they redshift into local Lyman resonance frequencies. Radiative cascades following the scattering of high order Lyman series photons will produce radiation from higher order hydrogen sequences like the Balmer and Paschen series (Meiksin 2010). The haloes will be highly extended because of the distances over which higher energy photons may travel before scattering. The H α signal from within the inner 1 arcminute of the halo could, as for the Ly α signal, be detected by an infra-red detector in space. The Balmer haloes, however, have the advantages over the Ly α haloes of being both more extended and comprised of multiple orders. Combining the images for the different resolvable orders could substantially reduce the required integration times for a given source.

Since the identical structures would give rise to a 21cm signature around a source (Madau et al. 1997; Pritchard & Loeb 2011), correlating the images with radio detections using an instrument like the LOw Frequency ARray (LOFAR)¹ or the Square-Kilometre Array (SKA)² would further enhance the detections and probe the structure of the underlying IGM as well as the ionization geometry produced by the source (Tozzi et al. 2000).

The purpose of this paper is to compute the expected Balmer signals allowing for the structure of the IGM. Since the scattering rate depends on the optical depth from the source to Lyman resonance line photons, the signal will

* Scottish Universities Physics Alliance

¹ www.lofar.org

² www.skatelescope.org

depend on the density, temperature and peculiar velocity structure of the IGM. The influence of inhomogeneities in these quantities is computed using a cosmological numerical simulation.

The paper is structured as follows: the next section summarises the mechanism of the effect and the simulation model. A presentation of the resulting images follows. The observational requirements for detecting the signal are then discussed, followed by our conclusions.

2 THE PRODUCTION OF BALMER HALOES

2.1 The Ly α scattering rate

The local Ly α radiation field within a gas parcel arises from two contributions, the direct UV photons emitted from the central radiating source redshifted to the local Ly α resonance frequency by the cosmological expansion and any radial peculiar velocity v_r of the gas, and the photons produced in radiative cascades following the scattering of higher order Lyman series photons. The effect of redshifting limits the distance freely streaming photons from a source may travel before scattering. From the perspective of a gas parcel at redshift z , only sources within the Lyman horizon

$$1 + z_n^{\text{horizon}} = (1 + z) \left(1 - \frac{v_r}{c}\right) \frac{1 - (n+1)^{-2}}{1 - n^{-2}}. \quad (1)$$

are able to excite a hydrogen atom into an electronic state with principal quantum number n (Barkana & Loeb 2005). Higher energy photons will have passed through a higher order Lyman resonance. As a result, the maximum possible distance of sources able to produce a direct scatter of Ly α photons decreases with increasing n .

Higher order Lyman photons will scatter within the Doppler core³. The mean free path of Ly α photon within the Doppler core is

$$\begin{aligned} \lambda_n^{\text{mfp}}(z) &= \frac{\pi^{1/2} \Delta\nu_{D,n}}{n_{\text{H}}(z) \sigma_n} \\ &\simeq 0.101(1+z)^{-3} T^{1/2} n(n^2 - 1) \text{ pc} \end{aligned} \quad (2)$$

where $n_{\text{H}}(z)$ is the hydrogen number density, $\Delta\nu_{D,n} = \nu_n b/c$ is the Doppler width with Doppler parameter $b = (2kT/m_{\text{H}})^{1/2}$ for gas temperature T , and $\sigma_n = (\pi e^2/m_e c) f_{1n}$ for oscillator strength f_{1n} (Meiksin 2009). The approximation $f_{1n} \simeq 1.56n^{-3}$ was used, accurate to better than 10 per cent. for $n > 4$. The mean free path is much smaller than the Jeans length $\lambda_J = c_s(\pi/G\rho_M)^{1/2} \simeq 16(1+z)^{-3/2} T^{1/2}$ kpc for a sound speed c_s and cosmic mass density ρ_M over which the physical properties of the IGM will be nearly uniform. The redistribution of photon energy from scatters may thus be considered to occur locally, confined within a homogeneous medium. A higher order photon will scatter only a few times before decaying into a lower order photon, with a survival probability of ~ 0.8 per scatter (Hirata 2006; Pritchard & Furlanetto 2006), so that the effects of spatial and frequency diffusion, redshifting and evo-

lution of the IGM will be negligible before the photon is destroyed.

Including photons produced in cascades from higher orders, the net scattering rate of Ly α photons is

$$P_n = \frac{1}{1 - p_{n,n}} \left[P_n^{(1)} + \sum_{n' > n}^{n_{\text{max}}} p_{n',n} P_{n'} \right], \quad (3)$$

for a maximum order n_{max} of directly scattered Lyman resonance line photons, where $P_n^{(1)}$ is the direct scattering rate

$$P_n^{(1)} = P_n^{\text{inc}}(0) \mathcal{S}_n, \quad (4)$$

with $P_n^{\text{inc}}(0) = \sigma_n L_{\nu_n} (4\pi r_L^2 h \nu_n)$ the scattering rate at the luminosity distance r_L from a source of specific luminosity $L_{\nu_n(1+z_s)/(1+z)}$ assuming no intergalactic attenuation (Meiksin 2010). Here, \mathcal{S}_n accounts for the intergalactic attenuation and $p_{n',n}$ is the probability that a Ly α photon converts to a Ly α photon per scatter.

The scattering rate may be expressed more succinctly in terms of the direct scattering rates as

$$P_n = \frac{1}{1 - p_{n,n}} \sum_{n'=n}^{n_{\text{max}}} \mathcal{C}_{n',n} P_{n'}^{(1)}, \quad (5)$$

where the scattering cascade matrix $\mathcal{C}_{n',n}$ has been defined according to

$$\mathcal{C}_{n',n} = \sum_{n'' > n}^{n'} \mathcal{C}_{n',n''} \eta_{n'',n}, \quad (6)$$

with $\mathcal{C}_{n,n} = 1$, $\mathcal{C}_{n',n} = 0$ for $n > n'$ and $\eta_{n'',n} = p_{n'',n}/(1 - p_{n'',n'})$.

The suppression factor \mathcal{S}_n is given by

$$\mathcal{S}_n = \int_0^\infty d\nu \varphi_{\nu_n}(a_n, \nu - \nu_n) e^{-\tau_n(\nu, z; z_s)}, \quad (7)$$

where $\varphi_{\nu_n}(a_n, \nu - \nu_n) = (\Delta\nu_{D,n})^{-1} \phi(x)$ is the Voigt profile with $x = (\nu - \nu_n)/\Delta\nu_{D,n}$ and a_n is the ratio between the damping width and Doppler width for Ly α photons. The optical depth is given by

$$\begin{aligned} \tau_n(\nu, z; z_s) &= \sigma_n \int_z^{z_s} dz' \frac{dl}{dz'} n_{\text{H}}(z') \\ &\quad \times \varphi_{\nu_n} \left[a_n(T'), \nu \frac{1 - v_r'/c}{1 - v_r/c} \frac{1 + z'}{1 + z} \right]. \end{aligned} \quad (8)$$

2.2 The halo emissivities

The emissivities depend on the populations $n_{n,l}$ of the excited states, where the subscripts indicate the principal quantum number and orbital angular momentum, respectively, of a given fine-structure state of an excited hydrogen atom. The equations governing the populations are, for the ground state n_1 ,

$$\frac{dn_1}{dt} = \sum_{n=2}^{n_{\text{max}}} n_{n,1} A_{n1,10} - n_1 \sum_{n=2}^{n_{\text{max}}} P_n, \quad (9)$$

and for excited states,

$$\begin{aligned} \frac{dn_{n,l}}{dt} &= n_1 P_n \delta_{l,1} + \sum_{n'=n+1}^{n_{\text{max}}} \sum_{l'=l\pm 1} n_{n',l'} A_{n'l',nl} \\ &\quad - n_{n,l} \sum_{n'=1}^{n-1} \sum_{l'=l\pm 1} A_{nl,n'l'}, \end{aligned} \quad (10)$$

³ At $z = 8$, for an IGM temperature $T > 10$ K (100 K), Ly δ (Ly γ) and higher order Lyman resonance line photons scatter in the Doppler core (Meiksin 2010).

where $\delta_{l,l'} = 1$ for $l = l'$ and vanishes otherwise. Here, $A_{nl,n'l'}$ is the spontaneous decay rate from level n, l to level n', l' .

The level populations will establish their steady-state values on the timescales P_n^{-1} . The system of steady-state equations is solved by

$$n_{n,l} = \sum_{n'=n}^{n_{\text{max}}} n_1 P_{n'} \frac{C_{n'1,nl}}{\sum_{n''=1}^{n-1} \sum_{l''=\pm 1} A_{nl,n'l''}}, \quad (11)$$

where $C_{n'l',nl}$ is the cascade matrix expressing the probability that an upper state n', l' cascades down to a lower state n, l via all possible transition routes. It is given by

$$C_{n'1,nl} = \sum_{n''=n+1}^{n'} \sum_{l''=\pm 1} C_{n'1,n''l''} \alpha_{n''l'',nl}, \quad (12)$$

with $C_{n'l',nl} = \delta_{l,l'}$, where $\alpha_{n'l',nl} = A_{n'l',nl} / \sum_{n''=1}^{n'-1} \sum_{l''=\pm 1} A_{n'l',n''l''}$ is the branching ratio from level $n'l'$ to level nl (cf. Osterbrock (1989)). The transition rates $A_{n'l',nl}$ are computed as in Meiksin (2010).

The resulting emissivity due to all transitions from n to n' with mean frequency $\nu_{nn'}$ is

$$\begin{aligned} \epsilon_{nn'} &= \frac{h\nu_{nn'}}{4\pi} \sum_l \sum_{l'=\pm 1} n_{n,l} A_{nl,n'l'} \\ &= \frac{h\nu_{nn'}}{4\pi} n_1 \sum_l \sum_{l'=\pm 1} \beta_{nl} \alpha_{nl,n'l'}, \end{aligned} \quad (13)$$

where $\beta_{nl} = \sum_{n'=n}^{n_{\text{max}}} P_{n'} C_{n'1,nl}$. The observed specific intensity is then

$$\begin{aligned} j_\nu &\simeq \int_0^\infty dz \frac{dl_p}{dz} (1+z)^{-3} \epsilon_{nn'}(l_p) \\ &\quad \times \varphi_{\nu_{nn'}} \left[\nu \left(1 + \frac{v_{\parallel}}{c} \right) (1+z) - \nu_{nn'} \right], \end{aligned} \quad (14)$$

for emission along the line-of-sight path l_p with line-of-sight velocity v_{\parallel} .

3 INFRA-RED EMISSION TOMOGRAPHY

The optical depth is sensitive to the density, temperature and peculiar velocity fields. As a consequence, fluctuations in these quantities between the source and a given gas parcel will produce fluctuations in the scattering rate through Eqs. (4) and (5). These in turn will produce fluctuations in the emissivity of the resulting cascade radiation, opening up the opportunity to measure the density, temperature and peculiar velocity fields on small scales surrounding a source.

3.1 Numerical simulation

In order to estimate the magnitude of the effect of the fluctuations on the received intensity, we use a numerical cosmological Λ CDM simulation of the IGM to compute the signal predicted from the surroundings of a source placed in the simulation volume. The simulation was run using version 1.0.1 of ENZO⁴ with the cosmological parameter values

⁴ Available from <http://lca.ucsd.edu>.

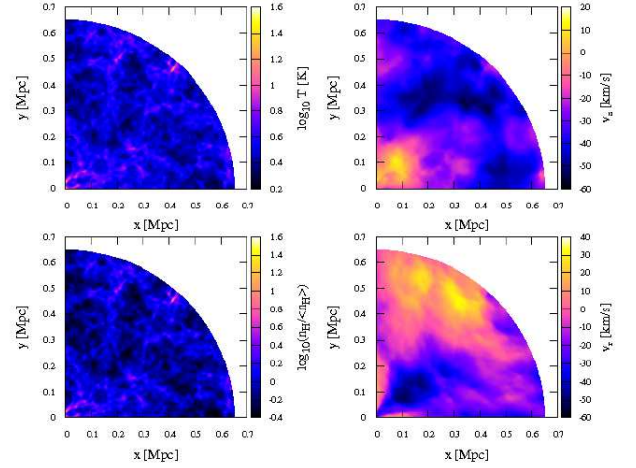


Figure 1. (Clockwise from the top left) The temperature, tangential (single component) peculiar velocity, radial peculiar velocity and density fields of IGM around a radiating source at the origin. (Distance units are proper.)

$\Omega_m = 0.236$, $\Omega_v = 0.764$ and $\Omega_b = 0.041$ for the matter, vacuum energy and baryonic matter density parameters, a Hubble constant $H_0 = 100h \text{ km s}^{-1} \text{ Mpc}^{-1}$ with $h = 0.73$, and the initial BBKS power spectrum with $n = 0.95$ normalised to $\sigma_8 = 0.74$, generally consistent with CMB fluctuations as measured by the *Wilkinson Microwave Anisotropy Probe* (Larson et al. 2011). The simulation was run in a volume $10h^{-1} \text{ Mpc}$ on a side with 256^3 cells and 512^3 dark matter particles. The volume was evolved from an initial redshift of $z_i = 530$ to $z = 10$. The initial mean temperature is set to $550 \text{ K} \left(\frac{1+z_i}{1+200} \right)^2 \simeq 3800 \text{ K}$, and evolves to $T \simeq 2 \text{ K}$ by $z = 10$. Radiative cooling permits collapse of gas in halos, but there is no feedback from star formation.

A source was assigned to the highest gas density peak within the simulation volume at $z = 10$, as recorded on the gas grid with cells of size $10/256 \text{ Mpc } h^{-1} \simeq 40 \text{ kpc } h^{-1}$ per side comoving. The corresponding density, temperature and peculiar velocity fields in a quadrant around the source are shown for a slice in Fig. 1, with representative line-of-sight values shown in Fig. 2.

The source is modelled as a starburst galaxy with a specific intensity approximated as flat at the relevant frequencies, so that the source intensity a luminosity distance r_L away is

$$\mathcal{S}_\nu = \frac{L_{\nu_L}}{(4\pi)^2 r_L^2} \quad (15)$$

where L_{ν_L} is the luminosity at the Lyman edge frequency ν_L . A continuous star formation rate $10M_\odot \text{ yr}^{-1}$ is assumed, with a Salpeter initial mass function for the range $1 < M < 100M_\odot$ and a metallicity $Z = 0.05Z_\odot$, corresponding to $L_{\nu_L} = 3.8 \times 10^{21} \text{ Js}^{-1} \text{ Hz}^{-1}$ after 10^7 yr (Leitherer et al. 1999).

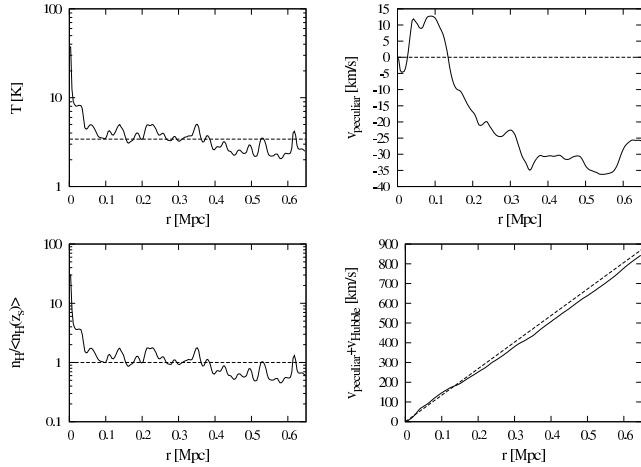


Figure 2. (Clockwise from the top left) Representative line-of-sight variations in the temperature, peculiar velocity, total velocity (including Hubble flow) and density of IGM around a radiating source at the origin. The dotted lines are the corresponding values for a homogeneous expanding medium. (Distance units are proper.)

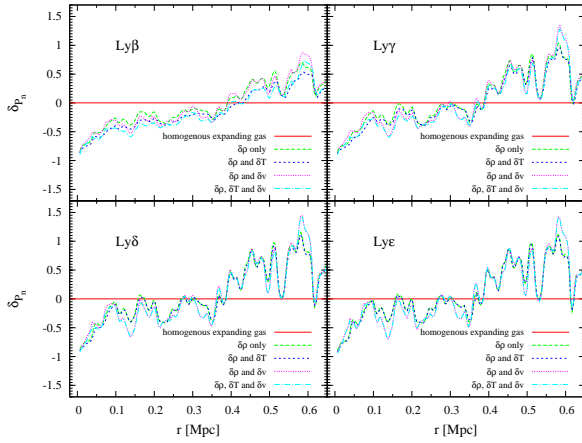


Figure 3. The relative difference between the $\text{Ly}\alpha$ scattering rate along the ray in Fig. 2 and the corresponding rate assuming a homogeneous expanding medium.

3.2 Emission line haloes

The resulting scattering rates of $\text{Ly}\alpha$ photons differ substantially from those for a homogeneous expanding medium, as shown in Fig. 3. The contributions due to the density, temperature and velocity departures from the mean are broken down in the figure. While the differences are primarily due to the density fluctuations, fluctuations in the temperature and expansion velocity contribute non-negligibly. In particular, the scattering rate becomes increasingly sensitive to the peculiar velocity field towards the higher orders, for which scattering in the Doppler core dominates increasingly over Lorentz wing scattering. As the optical depth increases with decreasing total velocity gradient, regions with a peculiar velocity gradient $dv/dr < 0$ tend to have a suppressed scattering rate compared with regions with $dv/dr > 0$. This may

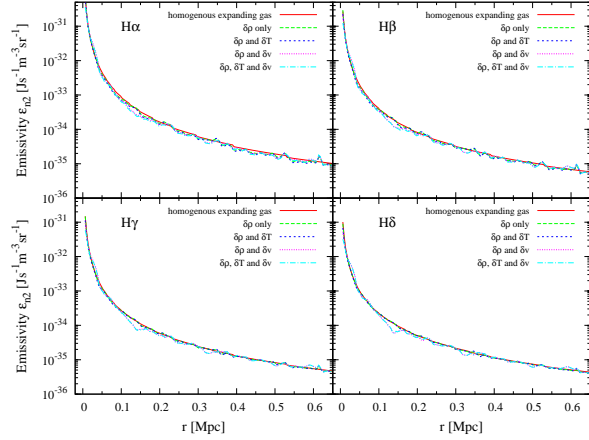


Figure 4. The relative difference between the $\text{H}n$ emissivity along the ray in Fig. 2 and the corresponding rate assuming a homogeneous expanding medium.

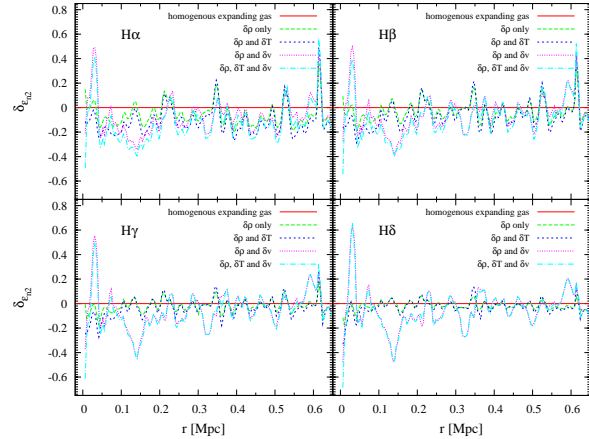


Figure 5. $\text{H}n$ emissivity along the ray in Fig. 2.

be seen by comparing the fluctuations in the scattering rate in Fig. 3 with the slope in the total velocity shown in the lower right panel of Fig. 2.

The Balmer emissivity profiles for $\text{H}\alpha$ through $\text{H}\delta$ are shown in Fig. 4 for the ray shown in Fig. 2. The fluctuations follow those in the $\text{Ly}\alpha$ scattering rates, but are somewhat suppressed in magnitude, as shown in Fig. 5. This is because, while the emissivity is proportional to the local gas density, so that fluctuations in the emissivity include a linear dependence on the density fluctuations, the scattering rate fluctuates oppositely to the density fluctuations because of the effect of the optical depth variations. The sum of the contributions to the relative fluctuations in the emissivity is thus reduced compared with the magnitude of the relative density fluctuations.

The derivation of the surface brightness is computationally intensive, as the cascade equations must be solved separately within each simulation cell. For this reason the computation is restricted to a plane perpendicular to the

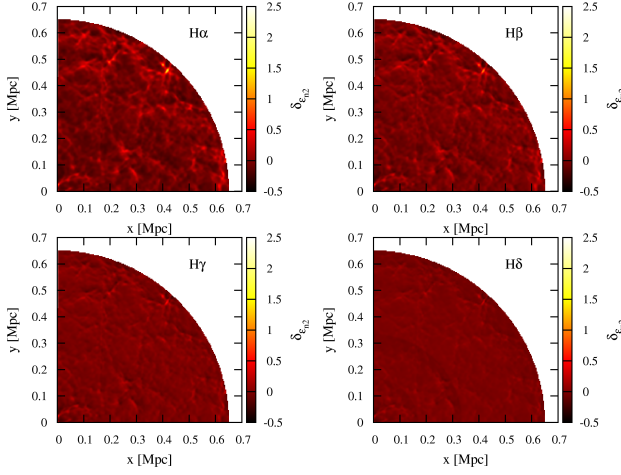


Figure 6. Differential Balmer surface brightness fluctuations compared with the homogeneous expanding IGM case allowing only for the density fluctuation contribution.

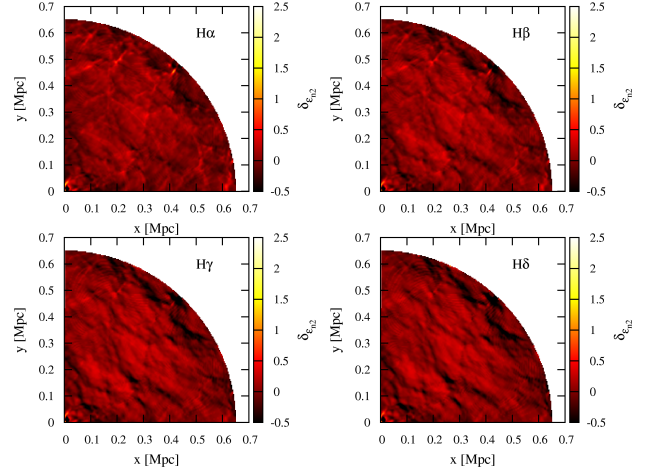


Figure 8. Differential Balmer surface brightness fluctuations compared with the homogeneous expanding IGM case allowing only for the density and velocity fluctuation contributions.

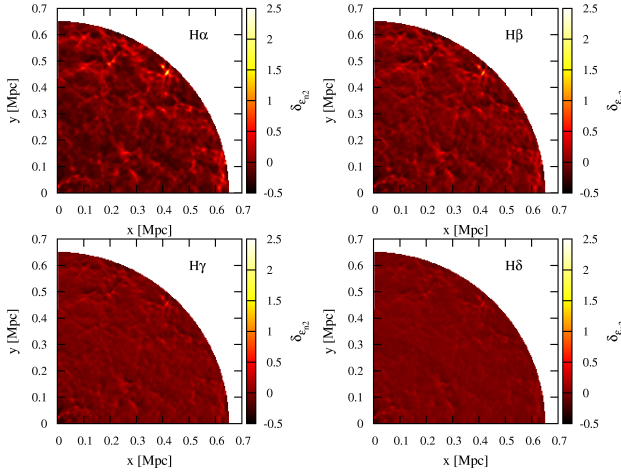


Figure 7. Differential Balmer surface brightness fluctuations compared with the homogeneous expanding IGM case allowing only for the density and temperature fluctuation contributions.

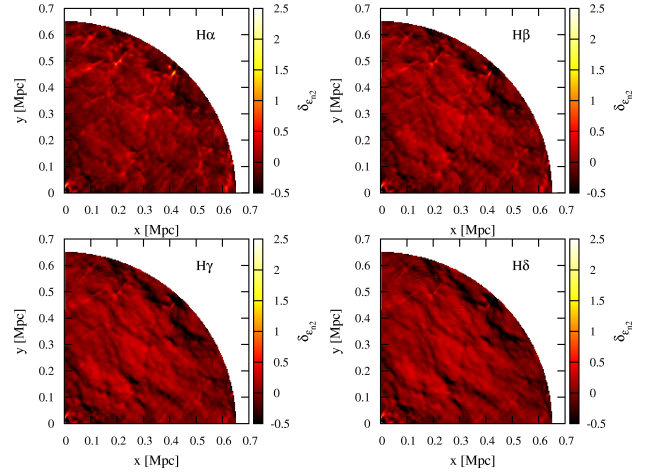


Figure 9. Differential Balmer surface brightness fluctuations compared with the homogeneous expanding IGM case allowing for the effects of density, temperature and velocity fluctuations.

line-of-sight. A narrow-band filter would include contributions from the nearby foreground and background regions as well. Modelling a specific filter arrangement would require further layers to be included for a realistic estimate, which would tend to blur the image if the filter width corresponded to a length scale that exceeds the coherence scale of the inhomogeneities. The results shown here are thus only representative of the magnitude of the effects that should arise from inhomogeneities in the density, temperature and peculiar velocity fields.

The effects of the density, temperature and velocity fluctuations on the Balmer surface brightnesses are illustrated in the differential maps shown in Figs. 6, 7, 8 and 9. The maps show the differences from the case for a homogeneous expanding IGM. The differential map allowing only for the density fluctuations shows the suppression by the increased optical depth in dense regions, as in Fig. 5. Adding in the contribution of the temperature fluctuations substantially enhances the structures. Adding the peculiar velocity contribution to the density emphasizes differentials in the struc-

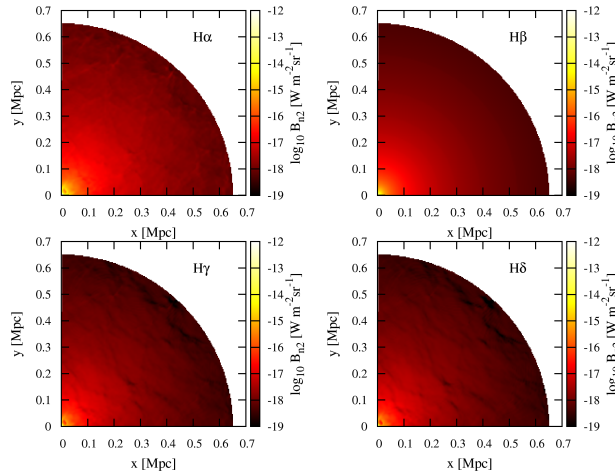


Figure 10. Balmer surface brightnesses including the effects of density, temperature and velocity fluctuations.

Source	H α 5.91 μm	H β 4.38 μm	H γ 3.91 μm	H δ 3.69 μm
Zodiacal	4.7×10^4	7.7×10^3	3.5×10^3	2.6×10^3
Halo	0.048	0.018	0.011	0.0089
SNR/ \dot{M}_{100}	$0.16 t_4^{1/2}$	$0.15 t_4^{1/2}$	$0.14 t_4^{1/2}$	$0.13 t_4^{1/2}$

Table 1. Estimated photon flux (photons $\text{m}^{-2} \text{s}^{-1}$) from low-level zodiacal light and the integrated halo flux within one arcmin of a starburst at $z = 8$, through an aperture of solid angle 4 arcmin² and narrow-band filter with resolution $\lambda/\Delta\lambda = 100$. The starburst is normalised to a star formation rate of $100\dot{M}_{100} M_{\odot} \text{yr}^{-1}$. The last row provides the signal-to-noise ratio after an integration time t_4 in units of 10^4 s for flux incident on a mirror and detector with effective collecting area 50 m². An IGM temperature $T = 10$ K is assumed.

tures, allowing the possibility of tracing the peculiar velocity field around forming galaxies on small scales.

The combined map is shown in Fig. 10. The rippling effect of the IGM is clearly discernable. The influence of the peculiar velocity becomes increasingly strong for the higher orders, where the dominant scattering producing the signals moves from the Voigt wings to the Doppler core.

4 DETECTION OF INFRA-RED EMISSION HALOES

The Balmer emission lines produced in the diffuse IGM by galaxies during the Epoch of Reionization will redshift to the infrared. In this section, an estimate is made for the requirements to detect the haloes. It is assumed the detector is limited by photon noise, which will be dominated by the IR background, primarily zodiacal light for a telescope in space. A fiducial collecting area of $A_{\text{fid}} = 50 \text{ m}^2$ is adopted

with a field of view of $\text{FOV}_{\text{fid}} = 2 \times 2 \text{ arcmin}^2$. Imaging using a narrow-band filter of resolution $R = \lambda/\Delta\lambda = 100$ is assumed.

Estimates for the zodiacal light background⁵ based on the model of Wright (1998) are converted to count rates in Table 1. The intensity of zodiacal light depends on the position and pointing direction of a satellite. The lower estimates are quoted here.

Lyman Break Galaxies and Ly α emitters at $z > 6$ suggest star formation rates of up to $30 M_{\odot} \text{yr}^{-1}$ (González et al. 2011; McLure et al. 2011). Much higher star formation rates are known in the lower redshift Universe, reaching values of $500 - 1000 M_{\odot} \text{yr}^{-1}$, but these are associated with ultra-luminous infra-red galaxies (ULIRGs) in dusty environments, which severely attenuate the ultra-violet radiation (Kennicutt 1998). On the other hand, by $z = 1 - 2$ ULIRGs are found to be much more transparent to UV radiation (Daddi et al. 2007). Accordingly, our estimates are normalized to a source with a star formation rate of $100 M_{\odot} \text{yr}^{-1}$.

The resulting lower order Balmer fluxes are shown in Table 1, based on the estimates in Meiksin (2010). The corresponding signal-to-noise ratios (SNR) after integrating over a time t are provided in the last row of the table. The SNR is nearly independent of the Balmer order. Increasing the resolution to $R = 500$ would be adequate for capturing the emitting flux while minimizing the zodiacal light background. A starburst as great as $700 M_{\odot} \text{yr}^{-1}$ would still be required to achieve a 3σ detection in 2×10^4 s. Allowing for the stacking of multiple bands in an instrument that split the beam into a range of bands tuned to correspond to the different Balmer series, would reduce the required star formation rate for detection by the square-root of the number of bands stacked.

The haloes could plausibly be detected by the *James Webb Space Telescope (JWST)* using the Tunable Filter Imager for a sufficiently bright source. The narrowest filter width, with resolution⁶ $R \simeq 100$, is sub-optimal, as it is broader than the emission feature, and thus lets in an excessive amount of background light compared with the signal. The wavelength range of the detector would also miss H α for a source at redshift $z_S > 6.6$, however it would capture the higher orders. The mirror has a collecting area of 25 m². Allowing for a photon throughput of 50 per cent., a 5σ detection of H β for a $1000 M_{\odot} \text{yr}^{-1}$ source would require an integration time of 4.7×10^5 s.

5 CONCLUSIONS

The search for the highest redshift galaxies may have identified forming galaxies responsible at least for a large component of the reionization of the intergalactic medium. Establishing that the IGM was actually neutral, however, requires direct detection of the neutral medium. A major goal of existing and planned radio facilities is to detect the neutral IGM 21cm signal from the Epoch of Reionization. A complementary path is to discover the UV light from the sources

⁵ At http://jwstet.stsci.edu/etcstatic/users_guide/t8_background.html.

⁶ At http://www.stsci.edu/jwst/doc-archive/handbooks/JWST_Primer_v20.pdf.

re-radiated by the IGM and received as infra-red radiation. Rescattered Ly α photons offer one possibility, although the emission is restricted by the spatial diffusion of the photons to the vicinity of the source. Higher energy photons will redshift into local higher order Lyman series photons, exciting extended Balmer and higher order emission line haloes through electron cascades following Lyman photon scattering.

We have shown that the fluctuations in the signal are sensitive not only to the density fluctuations in the surrounding gas through the mean free path of the scattered Lyman photons, but of the velocity field as well. This offers the possibility of mapping out both the ionization structure and the peculiar velocity field, produced by inflows or wind-driven outflows, surrounding the earliest major radiation sources, whether galaxies or AGN.

The principle obstacle to the detection of the infra-red haloes is the zodiacal light background. The ideal observing instrument would be a space telescope with an effective collecting area of 50 m², a field of view of a few to several square arcminutes, and a detector sensitive to the wavelength range 1–7 μ m with the capability of simultaneous imaging in several narrow tunable bands with a resolution of $R \simeq 500$. Basing an estimate on a pointing to a region of sky with a low-level of zodiacal light background, we find a 700 M $_{\odot}$ yr⁻¹ starburst galaxy could be detected at the 3 σ level in a single band in a 2×10^4 s integration, or a starburst of half the strength if observed simultaneously in four bands.

Although sub-optimal in design for this purpose, the Tunable Filter Imager on *JWST* could detect a $z = 8$ 1000 M $_{\odot}$ yr⁻¹ starburst galaxy at the 5 σ level in H β in a 5×10^5 s integration. While a major resource investment, it is half the time allocated to the *Hubble Space Telescope* Ultra-Deep Field and would offer the prize of a definitive detection of the Epoch of Reionization.

ACKNOWLEDGMENTS

K.K. acknowledges support from the Mie Prefecture of Japan for a Study-abroad Scholarship, and thanks the Robert Cormack Bequest for an Undergraduate Summer Vacation Research Scholarship. E.T. is supported by an STFC Rolling Grant.

REFERENCES

- Barkana R., Loeb A., 2005, *ApJ*, 626, 1
- Bouwens R. J., Illingworth G. D., Labbe I., Oesch P. A., Trenti M., Carollo C. M., van Dokkum P. G., Franx M., Stiavelli M., González V., Magee D., Bradley L., 2011, *Nature*, 469, 504
- Daddi E., Dickinson M., Morrison G., Chary R., Cimatti A., Elbaz D., Frayer D., Renzini A., Pope A., Alexander D. M., Bauer F. E., Giavalisco M., Huynh M., Kurk J., Mignoli M., 2007, *ApJ*, 670, 156
- González V., Labbé I., Bouwens R. J., Illingworth G., Franx M., Kriek M., 2011, *ApJ*, 735, L34
- Hirata C. M., 2006, *MNRAS*, 367, 259
- Kennicutt Jr. R. C., 1998, *ARA&A*, 36, 189
- Larson D., Dunkley J., Hinshaw G., Komatsu E., Nolte M. R., Bennett C. L., Gold B., Halpern M., Hill R. S., Jarosik N., Kogut A., Limon M., 2011, *ApJS*, 192, 16
- Leitherer C., Schaerer D., Goldader J. D., González Delgado R. M., Robert C., Kune D. F., de Mello D. F., Devost D., Heckman T. M., 1999, *ApJS*, 123, 3
- Loeb A., Rybicki G. B., 1999, *ApJ*, 524, 527
- Madau P., Meiksin A., Rees M. J., 1997, *ApJ*, 475, 429
- McLure R. J., Dunlop J. S., de Ravel L., Cirasuolo M., Ellis R. S., Schenker M., Robertson B. E., Koekemoer A. M., Stark D. P., Bowler R. A. A., 2011, *MNRAS*, 418, 2074
- Meiksin A., 2010, *MNRAS*, 402, 1780
- Meiksin A. A., 2009, *Reviews of Modern Physics*, 81, 1405
- Ono Y., Ouchi M., Mobasher B., Dickinson M., Penner K., Shimasaku K., Weiner B. J., Kartaltepe J. S., Nakajima K., Nayyeri H., Stern D., Kashikawa N., Spinrad H., 2012, *ApJ*, 744, 83
- Osterbrock D. E., 1989, *Astrophysics of gaseous nebulae and active galactic nuclei*. University Science Books, Mill Valley, CA
- Pritchard J. R., Furlanetto S. R., 2006, *MNRAS*, 367, 1057
- Pritchard J. R., Loeb A., 2011, *ArXiv e-prints*, 1109.6012
- Schenker M. A., Stark D. P., Ellis R. S., Robertson B. E., Dunlop J. S., McLure R. J., Kneib J.-P., Richard J., 2012, *ApJ*, 744, 179
- Tozzi P., Madau P., Meiksin A., Rees M. J., 2000, *ApJ*, 528, 597
- Vanzella E., Pentericci L., Fontana A., Grazian A., Castellano M., Boutsia K., Cristiani S., Dickinson M., Galozzi S., Giallongo E., Giavalisco M., Maiolino R., Moorwood A., Paris D., Santini P., 2011, *ApJ*, 730, L35
- Wright E. L., 1998, *ApJ*, 496, 1